Impact-collision ion-scattering spectroscopy of Cu(110) and Cu(110)-(2×1)-O using 5-keV $^6Li^+$

Jory A. Yarmoff,* Donna M. Cyr,† Judy H. Huang, Sehun Kim, and R. Stanley Williams
Department of Chemistry and Biochemistry, University of California, Los Angeles, California 90024
(Received 9 September 1985)

Impact-collision ion-scattering spectroscopy was performed using 5-keV $^6Li^+$ ions to study the Cu(110) and Cu(110)-(2×1)-O surfaces. Polar-angle scans were collected for scattering along the [1$\bar{1}$0], [1$\bar{1}$2], and [001] azimuths. These scans were quantitatively analyzed by comparing them to the results of an algorithm that combined a one-atom Monte Carlo computer simulation with various structural models to calculate trial polar scans. The results for the clean surface support a model in which the first- to second-atomic-layer spacing was contracted (10±5)% compared to the bulk spacings and the vibrational amplitudes of the atoms in the outermost atomic layer were enhanced by a factor of 1.5 over the bulk vibrational amplitude. For a surface with a 200 L oxygen exposure (1 L≡10^{-6} torr sec), the results were not consistent with a buckled-row model, but indicated that every other [001] atom row was missing, the first-to second-layer spacing was expanded (25±10)%, and the second- to third-layer spacing was contracted (10±5)%. At higher oxygen exposures, the surface Cu layer became disordered.

I. INTRODUCTION

Low-energy ion-scattering spectroscopy (LEIS), also referred to as ion-scattering spectroscopy, has been used over the past 15 years as a means for determining the atomic composition and more recently the structure at a single-crystal surface.[1–7] Aono has introduced a new form of LEIS, impact-collision ion-scattering spectroscopy (ICISS), for which the analysis that is necessary to produce a structural determination is greatly simplified.[8–12] The basic experimental method of the ICISS technique is to monitor the intensity of the quasi-singly (QS) scattered ions as a function of the incident ion-beam direction with respect to the sample orientation for ions that have scattered at an angle close to 180°. With such a scattering angle, the backscattered ions retrace almost the same path as the incident ions. The assumption is therefore made that if an ion is able to penetrate into the crystal and suffer only one large angle collision, it can then escape the crystal and reach the detector without interacting with other atoms. The analysis of ICISS data thus becomes a determination of the total flux of ions at the incident ion-beam energy to reach each of the target atoms.

The usual method for ICISS data analysis involves the concept of the shadow cone,[13] which is the region behind a target atom from which the ions are deflected. The ion flux at the edge of a shadow cone is enhanced over the incident flux by small-angle scattering that transfers very little energy from the projectiles. This enhanced flux can thus be considered to be at the incident ion energy. In ICISS, as the sample is rotated with respect to the incident ion-beam direction, the intensity of the ion flux that reaches atoms located behind other atoms that are directly exposed to the ion beam varies greatly. Depending on their relative orientation, one atom may be completely shadowed from the ion beam by another, or an atom may experience a considerably enhanced ion flux if it is located at the edge of the shadow cone of another.

When an atom is located in the center of a shadow cone, there can be no direct scattering from that atom into the detector. When the incident ion-beam direction is rotated with respect to the sample, the position of the shadowed atom is rotated towards the edge of the shadow cone. The flux of ions to reach the initially shadowed atom rises to a maximum, and then falls to the level of the incident ion flux after the atom has been rotated sufficiently far from the shadow cone. The distribution of the flux enhancement at the edge of a shadow cone is thus observed as a flux peak in an ICISS angular scan because there are more ions at approximately the incident ion energy that can scatter from the initially shadowed atom into the detector. The detailed shape of an observed flux peak depends on both the flux distribution at the edge of the shadow cone and the interatomic spacing and angle between the two atoms involved. Therefore, if the flux distribution at the edge of a shadow cone is determined, it can be used in conjunction with a model for the atomic structure of a given surface to calculate the shape of an ICISS angular scan.

In most previous studies, the detailed flux distribution at the edge of a shadow cone was not calculated.[8,10,12] Instead, a critical angle was defined to be fixed at some point that corresponded to a certain height above background (e.g., one-half of the peak height) of the observed shadowing flux peak. The expected shadow-cone shape can be determined experimentally from features in angular scans that resulted from known parts of the surface structure, i.e., the parallel distances between atoms along various azimuths for a surface with a 1×1 low-energy electron-diffraction (LEED) pattern.[8,12] The shadow-cone shape measured in this way can then be used to determine the unknown portion of the structure that was responsible for the other features in the scan. This procedure assumes that a shadow-cone shape defined in this way will be invariant when applied to different atoms in a crystal. It is known, however, that surface atoms may exhibit very dif-

ferent vibrational amplitudes than bulk atoms, and the detailed shape of the average flux distribution at the edge of a shadow cone is dependent on the vibrational amplitude of the atom. Also, there is the possibility that there will be no known interatomic separations in a particular surface under examination, such as a surface that does not have a 1×1 LEED pattern. In one previous study, the shape of the flux enhancement was obtained via a Monte Carlo computer simulation modeled by a string of atoms.[11] This resulted in very good agreement with the experimental data, but the time required to produce an ICISS polar scan via this type of computer simulation is large because a complete simulation must be performed for each incident ion-beam direction.

Both noble-gas ions[8–11] and alkali-metal ions[12] have been employed as projectiles in ICISS studies. The main difference in the scattering behavior of noble-gas ions and alkali ions is the path-dependent neutralization exhibited by noble-gas ions.[14] Since the overall neutralization rate is much larger for noble-gas ions than for alkali ions, and the detectors employed in ICISS are sensitive only to the ion portion of the backscattered yield, the total amount of incident ion flux necessary to obtain results with a reasonable signal-to-noise level is much greater for noble-gas ions than for alkali ions. Too large an incident ion dose can produce a damaged surface before the scan is complete. Also, the neutralization probability for noble-gas ions increases as the ion-beam incidence angle with respect to the sample surface decreases. This can have the effect of attenuating features that result from surface atomic alignments to the point where they are not distinct enough to be used for a structural determination.[15] For scattering from Cu, the neutralization probability for He^+ is fairly high,[16] and therefore Li^+ ions were chosen in order to perform structural determinations at the Cu(110) surface.

A previous study of ICISS on Cu(110) was performed by Niehus and Comsa using 2-keV $^{23}Na^+$ projectiles.[12] The use of the smaller incident energy and the larger projectile atomic number in Ref. 12 produced very different ICISS angular scans than those in the present study. The flux peaks from 2-keV $^{23}Na^+$ were smaller and less distinct than the flux peaks from 5-keV $^6Li^+$. Because of this, the data reported in Ref. 12 were less sensitive to the quantitative details of the Cu(110) surface than the ICISS scans presented in this study.

The clean Cu(110) surface has also been studied with Rutherford backscattering (RBS) (Ref. 17) and LEED.[18–20] The results of these studies have indicated that the Cu(110) surface exhibits an oscillatory relaxation in which the first- to second-atomic-layer spacing is contracted and the second to third layer is expanded. The values reported for the first-layer contraction ranged from 5.3% of a bulk interlayer spacing to 8.5%.

A LEIS study of the Cu(110)-(2×1)-O surface has indicated that the O sits in the long bridge position 0.6 Å below the top atomic layer of Cu.[21–23] These studies have also shown that the oxygen induces a reconstruction of the Cu in which every other [001] row of Cu atoms becomes vacant. This missing-row model has been confirmed by ICISS (Ref. 12) and He atom diffraction.[24] The results of a RBS study[25] and an angle-resolved ultraviolet photoemission study,[26] however, have favored a buckled-row model in which every other [001] row is shifted vertically with respect to each other.

In this paper, we present experimental ICISS data for the scattering of 5-keV $^6Li^+$ from Cu(110) and Cu(110)-(2×1)-O. The use of a higher incident energy than in previous ICISS studies resulted in the formation of shadow cones with smaller diameters. This, in turn, increased the depth penetration of the projectiles into the solid and resulted in the formation of features in the ICISS scans that involved deeper-lying atoms than did previous studies. One consequence of scattering from more deeply lying atoms is that flux peaks from several different atom pairs in the near surface region may overlap.

The analysis of the data was performed by calculating the flux at the edge of each shadow and blocking cone from the results of a one-atom Monte Carlo computer simulation. This simple method of data analysis used only a small amount of computer time, but it did model the flux distribution at the edges of shadow and blocking cones as a function of both vibrational amplitude and interaction potential. The flux enhancement for each atom pair contributing to a particular feature in an ICISS scan was calculated separately, and then the results for each atom pair were summed together in a way that corresponded to a model for the surface structure. This calculated ICISS scan was compared with experiment, and then the structural parameters in the model surface were adjusted until a reasonable agreement between the calculation and the experiment was achieved.

In the present study, the results obtained for the Cu(110) clean surface indicate that the outermost atomic layer was relaxed inward $(10\pm5)\%$ of a bulk spacing. The results for Cu(110)-(2×1)-O reconstruction are consistent with a missing-row model in which the top atomic layer of Cu atoms is relaxed outward $(25\pm10)\%$ from the second layer and the second- to third-layer spacing is contracted $(10\pm5)\%$. The adsorption of large amounts of oxygen produced an ICISS scan resembling that previously observed from a disordered Cu(110) surface.[27]

In the next section, the details of the experimental procedure are described. The experimental results are presented in Sec. III and the algorithm for calculating ICISS polar scans is explained in Sec. IV. Section V discusses the use of the calculations and experimental data to obtain structural information about the clean Cu(110) and Cu(110)-(2×1)-O surfaces. Finally, the main conclusions of this work are presented in Sec. VI.

II. EXPERIMENTAL PROCEDURE

The Cu sample was oriented with Laue x-ray diffraction and cut from a boule of 99.998%-purity single-crystal Cu purchased from Atomergic Chemetals Corp. (Plainview, New York). After cutting with a wire saw, the sample was mechanically polished with successively finer grits of alumina down to 0.05 μm. The sample was then chemomechanically polished with an acid solution containing a mercapto-sulfur compound.[28] It was found that the best results were achieved if several alternating

cycles of mechanical polishing with 0.05-μm alumina and chemomechanical polishing with the acid solution were performed prior to installing the sample in the ultrahigh-vacuum (UHV) chamber. The sample was mounted on a sample manipulator that allowed both polar and azimuthal rotations, translations along three orthogonal axes, and adjustment of the sample tilt angle with respect to the ion-beam incidence direction.

The experiments were performed in an ion-scattering apparatus that will be described in detail elsewhere.[29] The two-level UHV chamber had a base pressure of 2×10^{-11} torr (after correcting for the x-ray limit of the ion gauge). During the ion-scattering measurements, the pressure rose to about 4×10^{-11} torr. The upper level of the UHV chamber contained an ion bombardment gun for sample cleaning and optics for low-energy electron-diffraction. The LEED optics were also used as a retarding-field analyzer for performing Auger electron spectroscopy (AES) to monitor the sample cleanness. The lower level of the UHV chamber was used for the ion-scattering experiments.

The ion accelerator produced a beam with a typical current of 1—5 nA in a 1-mm-diam spot size with an angular divergence of $\pm0.7°$. The scattered ions were detected with a hemispherical electrostatic analyzer (ESA) that was mounted on a rotatable turntable that allowed scattering angles from 0° to 166° to be obtained. All of the ICISS measurements reported here were obtained at a 166° scattering angle. The ESA was operated in the constant pass energy mode, with a typical pass energy of 1000 eV, which resulted in an energy resolution of ±15 eV. In addition to the ICISS measurements, polar-angle scans were performed using a 40-mm-diam dual microchannel plate (MCP) array as the detector. This wide-area detector collected ions scattered at angles from 110° to 160° with sufficient energy to initiate multiplication in the MCP.

Inside the UHV chamber, the sample was cleaned with cycles of 1-keV argon ion bombardment followed by annealing. It was determined that one anneal up to 550 °C for 30 min was necessary to produce a well-ordered surface, but after annealing to this temperature there was a strong sulfur AES signal. Therefore, after the 550 °C anneal, another cycle of ion bombardment followed by annealing to 400 °C was performed. All of the subsequent cleaning cycles involved anneals to 400 °C. Prior to each ICISS scan, the sample was ion bombarded and annealed, the surface composition was checked with AES, and the ordering of the surface was checked with LEED. The LEED was also used to align the azimuthal orientation of the sample prior to each ICISS polar scan. The existence of certain features in the ICISS polar scans was the final determination of the degree of ordering at the surface.[27]

An energy spectrum of the backscattered ions at normal incidence was obtained to determine the energy of the quasi-singly scattered $^6Li^+$ ions. After this spectrum was known, the analyzer energy was set to the energy of the maximum intensity in the QS scattering peak, and an ICISS polar scan was collected. The polar scan was performed by setting an angle on the sample manipulator and then counting the scattered ions for a specified period of time, typically 5 sec. The scattered ion intensity was determined for ion-beam incidence with respect to the sample from a polar angle of 0° (ion beam parallel to the sample surface) to 90° in 1° increments.

The oxygen exposures were carried out by leaking oxygen continuously into the UHV chamber while pumping on the chamber with a turbomolecular pump and maintaining a constant oxygen pressure of 1×10^{-6} torr. Oxygen exposures from 200 to 1200 L were studied. After each oxygen exposure, the sample was annealed to 100 °C for 5 to 10 min until a sharp 2×1 LEED pattern was observed.

III. RESULTS AND QUALITATIVE ANALYSIS

ICISS polar scans were collected for scattering along the [1$\bar{1}$0], [1$\bar{1}$2], and [001] azimuths. Figure 1 shows a top view of the Cu(110) surface with these directions indicated. The larger circles in Fig. 1 represent atoms in the plane of the surface and the smaller circles represent atoms in the second layer of the crystal. For scattering along the [1$\bar{1}$2] azimuth, all the atoms of the crystal lie in equivalent planes that are perpendicular to the surface. For both the [1$\bar{1}$0] and [001] azimuths, however, the atoms comprise two inequivalent alternating planes. One set of these planes is terminated by surface-layer atoms, while the other is terminated by second-layer atoms.

Figure 2 shows the ICISS polar scans obtained using 5-keV $^6Li^+$ as the projectile for scattering along each of these azimuths. These scans were aligned in intensity to each other at an ion incidence polar angle of 90°. At that point, since the ion beam was normal to the surface, the scattered intensity was essentially independent of azimuthal orientation. However, the backscattered ion intensity for polar angles less than 70° is strongly dependent on the

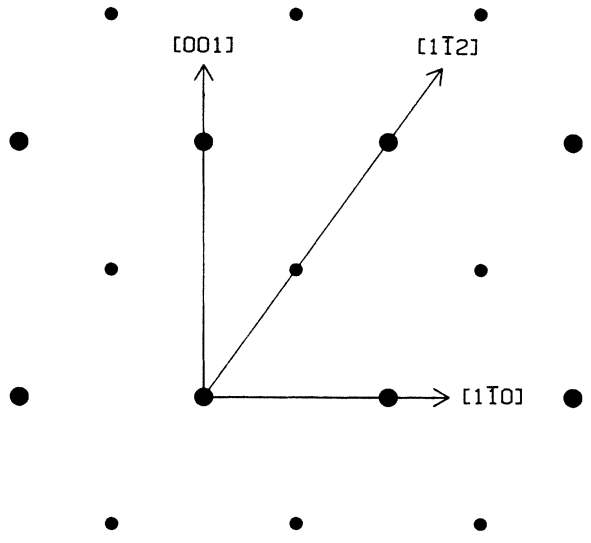

FIG. 1. Top view of the Cu(110) surface showing the azimuthal directions along which the ICISS polar scans were collected. The top two atomic planes are represented. The radii of the circles are drawn to represent the vibrational amplitudes of the atoms, and thus the surface atoms are represented by larger circles.

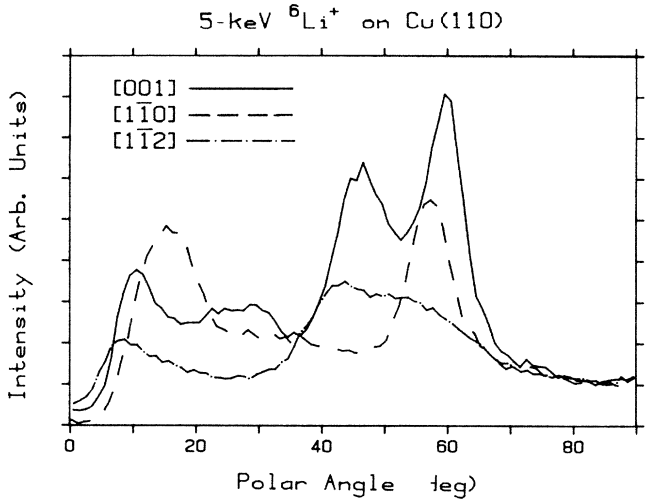

FIG. 2. ICISS polar scans for 5-keV $^6Li^+$ scattering from Cu(110) along the azimuths noted. The polar angle is measured between the incident ion beam and the sample surface. The scans were normalized in intensity to each other at 90°, where the scattering intensity should be essentially independent of azimuthal orientation.

azimuthal orientation.

In Fig. 2 the intensity maxima, or ion-scattering flux peaks, arise because of the existence of an alignment of two atoms that is repeated across the crystal surface. One of these atoms creates a shadow cone, and the enhanced flux at the edge of this shadow cone is focused onto the second atom at certain ion-incidence directions with respect to the atom pair. These focused ions are observed when they are backscattered from the second atom into the detector. Alternatively, a flux peak may be observed when an ion backscatters from a deep-lying atom, and then interacts with a less deeply lying atom along the exit trajectory, forming a blocking cone. Backscattered ion flux is concentrated at the edge of a blocking cone, which also leads to a flux peak in an ICISS scan when the edge of the blocking cone is rotated through the detector acceptance angle.

The first feature in each polar scan resulted from the atom pairs lying in the plane of the surface and is therefore referred to as the surface flux peak (SFP). The [1$\bar{1}$2] azimuth had only the outermost atomic layer contributing to the SFP, while the other two azimuths had contributions from both the first and second layers in the SFP. The onset of the SFP occurred at increasing polar angles for the [1$\bar{1}$2], [001], and [1$\bar{1}$0] azimuths (see Fig. 2). This order coincides with decreasing interatomic separations along these azimuths (4.42, 3.61, and 2.55 Å, respectively). Thus it can be seen that the angular position of an ICISS flux peak is dependent on the interatomic separation of the atom pairs responsible for the flux peak.

The polar scans shown in Fig. 2 did not fall to zero intensity at a polar angle of 0°, although at 0°, all of the atoms in the surface were well within the shadow cones of other atoms. The reason for this was that when the sample surface was parallel to the ion beam, the edge of the sample was also visible to the beam. Since the edge of the sample contained Cu atoms, there was scattering at the QS energy observed at that point.

All of the ICISS polar scans collected showed a blocking cone centered at a polar angle of approximately 80°. This blocking cone resulted from ions that had scattered from third- or deeper-layer atoms, and were blocked from exiting the crystal in the direction normal to the sample by atoms that were directly above the original scattering atom. The blocking cone shapes are determined as a function of the detector angle with respect to the surface, not the ion-beam incidence angle, since the flux enhancements at the edge of the blocking cones occurred along the scattered trajectory, not the incident trajectory. This implies that the blocking cones are centered about a polar angle of 76° in Fig. 2, i.e., the sample normal points directly at the detector when the ion beam is 76° away from the sample surface, since the ion beam and detector are 14° apart. The local minimum in the ICISS polar scan actually appeared at a polar angle of 83°, however, which is the point at which the ion beam and detector were located at a symmetric position 7° on either side of the sample normal, because at this point the shadowing and blocking flux enhancements were both at a minimum.

The blocking flux peak displayed a maximum at a beam incidence polar angle of approximately 60° for each azimuth, but the shapes of the blocking flux peaks were considerably different along each azimuth. The most obvious differences among the scattering trajectories that contributed to the blocking flux peaks along the different azimuths are the penetration depths of the ions. The more widely spaced the rows of atoms perpendicular to the surface are along a particular azimuth, the easier it is for ions to penetrate into the crystal and escape after backscattering from an atom. Thus, the number of target atoms contributing to the various subsurface flux peaks shown in Fig. 2 increases with increasing separation between the rows of atoms.

All the observed flux peaks in the ICISS polar scans resulted from atomic alignments in which the atom pair was directly visible to the incoming ion beam, i.e., the atoms involved were not shadowed by other atoms and the exit path was not blocked. The use of alkali ions rather than noble-gas ions and the use of higher energies than in previous ICISS studies resulted in these flux peaks being more pronounced than in previous studies, because the flux peaks had contributions from deeper atomic layers. A qualitative assignment of the flux peaks to certain atom pairs is possible by simple geometric analysis. However, because several atom pairs may have overlapping flux peaks, a calculation is necessary to determine whether or not a particular atom pair contributed to a particular flux peak. These calculations are discussed in the following sections.

Figure 3 shows polar scans collected with the wide-area detector along with the ICISS scans collected along the same azimuths. Because the wide-area detector collected particles that had scattered at all energies, the observed intensity contains mostly multiple-scattering trajectories, as opposed to the ICISS scans, which reflect QS scattering only. The wide-area detector scans reveal channeling

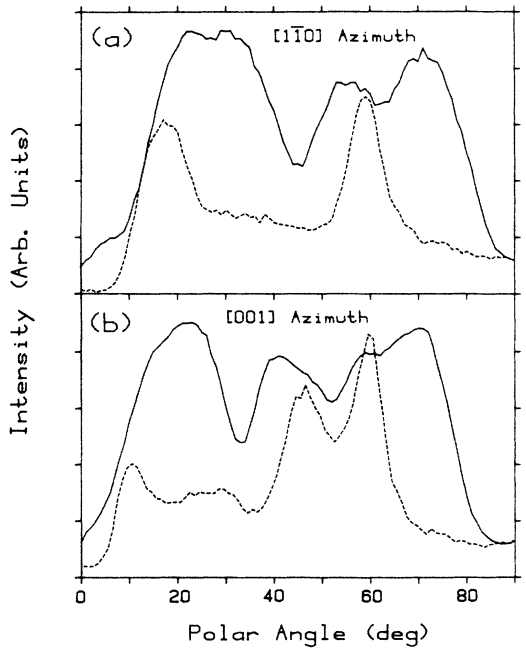

FIG. 3. Polar scans for 5-keV $^6Li^+$ scattering from Cu(110). The dashed curves show the ICISS polar scans and the solid-curves show the total scattered yield collected with the wide-area detector as a function of the incidence polar angle (a) along the [1$\bar{1}$0] azimuth, and (b) along the [001] azimuth.

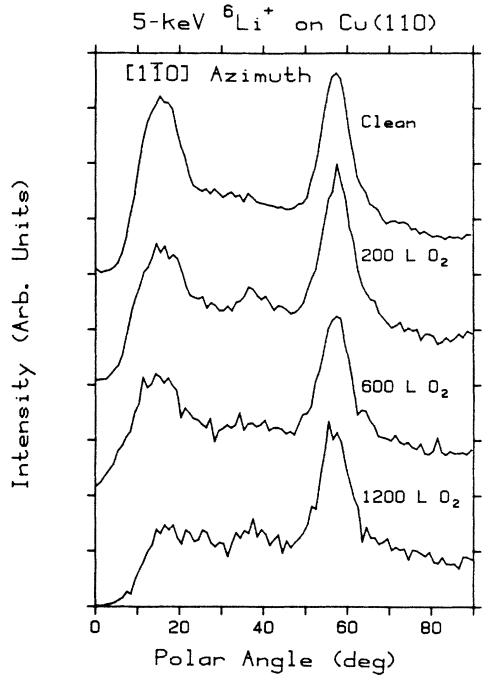

FIG. 4. ICISS polar scans of 5-keV $^6Li^+$ scattering from Cu(110) and Cu(100)-(2×1)-O along the [1$\bar{1}$0] azimuth for various oxygen exposures.

minima that correspond with bulk crystalline axes.[30] For both the ICISS scans and the wide-area detector scans, a local scattering minimum occurs in the vicinity of 90°. The wide-area scans are peaked at every angle at which the ICISS scans are peaked and also at angles with no ICISS flux peaks, but the peaks in the wide-area scans are much broader than the ICISS features.

Figure 4 shows the effects of adsorbing oxygen onto the sample on the ICISS scan along the [1$\bar{1}$0] azimuth. Each of the oxygen-covered samples displayed a sharp 2×1 LEED pattern before the ICISS scan was collected. A 200-L oxygen exposure reduced the intensity and increased the width of the SFP, and caused a small peak to appear at approximately 38°. The appearance of this peak indicates that a new atom pair had become visible to the ion beam. As the oxygen exposure was increased, the intensity of the SFP decreased and the peak at 38° disappeared. After the adsorption of 1200 L, the SFP was attenuated to the point where the polar scan appeared to be almost identical to a polar scan collected from a disordered Cu(110) surface.[27] The oxygen exposure did not noticeably reduce the size of the flux peak at a polar angle of ~58°.

IV. COMPUTATIONAL SIMULATION OF ICISS POLAR SCANS

The modulations in an ICISS polar scan result from both the interaction of an atom with the enhanced flux at the edge of a shadow cone of another atom and from the enhanced flux at the edge of a blocking cone. To model the effects of the enhanced flux at the edge of a shadow cone, only the flux of ions that reaches the second atom need be calculated, since the scattering angle, and therefore the cross section for backscattering from the second atom into the detector, is fixed in ICISS. The angular dependence of the flux enhancement at the edge of a blocking cone is displayed directly in an ICISS polar scan. Therefore, if the flux at the edge of each shadow and blocking cone in a particular model of a surface structure is calculated, a model ICISS polar scan can be constructed simply by summing the flux distributions from each atom pair that contributes to the particular ICISS polar scan.

A one-atom Monte Carlo computer simulation was used to calculate the flux distribution at the edges of shadow and blocking cones. The interaction potential used in the simulation was the Molière potential with an adjustable screening length, as in previous simulations of low-energy ion scattering.[31] The scattering trajectories for each one-atom simulation were maintained within a two-dimensional plane. A series of incident trajectories was run for impact parameters b, measured with respect to the equilibrium position of the atom, ranging from $b=0$ to the largest interatomic distance of all the atom pairs that would be used to model the surface structure. The spacing between each incident trajectory used in these calculations was 0.0001 Å. Before a scattering event was calculated, the atom was moved a randomly chosen distance in each of two orthogonal directions in the scattering plane to simulate thermal vibrations. The distance moved was chosen from a Gaussian distribution with a mean-square vibrational amplitude that was varied to produce a reasonable fit to the experimental data, as discussed below.

The results of the one-atom Monte Carlo simulation

were stored in a data file as the initial (nonvibrated) impact parameter b, the delta value Δ, and the scattering angle α. These variables are indicated in Fig. 5. In both Figs. 5(a) and 5(b), the initial and scattered velocity vectors are indicated by heavy lines with arrows. The delta value is the distance between the intersection of the ingoing and outgoing velocity vectors and the perpendicular drawn from either the shadowing or blocking atom position to the continuation of the initial velocity vector.

Ions that form a shadow cone begin as a set of parallel trajectories that are incident on each atom visible to the ion beam. To calculate the shape of a flux peak resulting from the enhanced flux at the edge of a shadow cone, each initial trajectory in the one-atom data file was assumed to represent a possible incident trajectory. For a fixed distance between the two atoms D, the angle θ_s, shown in Fig. 5(a), between the incident velocity vector and the line connecting the two atoms was calculated for each scattering event in the one-atom simulation data file. The equation relating θ_s to the known variables, b, Δ, α, and D, which was derived using the law of cosines, is as follows:

$$\theta_s = \alpha + \arcsin\{\cos(\alpha)[b + \Delta\tan(\alpha)]/D\} . \quad (1)$$

The total flux incident on the scattering atom as a function of θ_s was determined by summing the number of trajectories in 1° intervals into a histogram. The implicit assumption used here is that the energy of an ion scattering from the second atom into the detector will be close enough to the QS value to be within the resolution of the ESA. This approximation is very good for large total scattering angles and small initial scattering angles α. These calculations were normalized so that the scattered ion intensity from a single atom without flux enhancement was given a value of one.

To calculate blocking flux distributions, each event from a one-atom simulation data file, which was constructed using the energy that an ion would retain after making a single collision at the experimental scattering angle, was considered to be a trajectory originating at a point source located at the scattered atom and then interacting with the blocking atom. The angle θ_b, shown in Fig. 5(b), is the angle between the line connecting the scattering and blocking atoms and the final scattered trajectory:

$$\theta_b = \alpha + \arcsin(b/D) . \quad (2)$$

The blocking flux as a function of θ_b was also determined by summing trajectories into a histogram at 1° intervals.

For a given model of a surface structure, the flux distributions from each atom pair were summed by adding together the histograms from each individual flux distribution calculation. For atomic alignments in which the atoms were in the plane of the surface, the angle θ_s from the shadowing calculations was the polar angle as defined by the experiment. For atomic alignments at some other angle with respect to the plane of the surface, the angle between the line connecting the atom pair of interest and the surface plane must be added to θ_s to produce the polar angle. The angle θ_b that resulted from blocking calculations was related to the angle of the detector with respect to the interatomic vector, and therefore a 14° offset, the angle between the incident ion beam and the detector, was subtracted from θ_b to produce the polar angle.

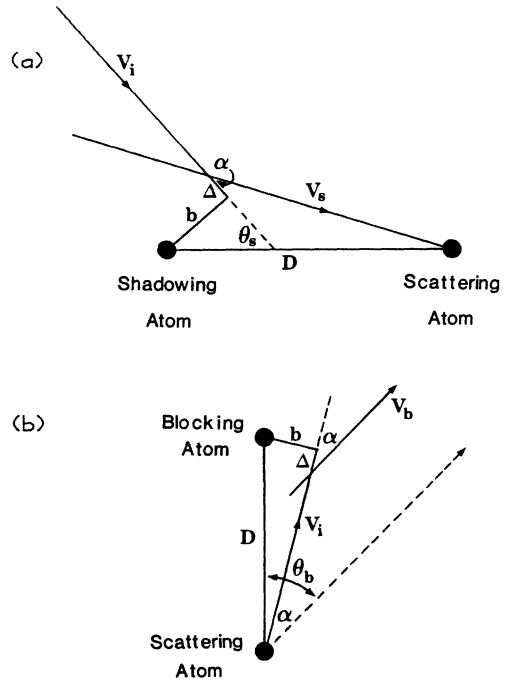

FIG. 5. Geometrical construction used for calculating the shadowing and blocking flux enhancements from a set of ion trajectories containing the initial impact parameter b, the scattering angle α, and the delta value Δ, for (a) a shadowing orientation with angle θ_s between the incident ion direction and the line connecting the atom pair, and (b) a blocking orientation for an angle θ_b between the line connecting the atom pair and the detector direction.

In this calculation, the vibrational displacements were applied only to the atom forming the shadow or blocking cone during the one-atom Monte Carlo simulation. To model correctly the vibrational amplitudes of an atom pair when one of the atoms was fixed in space, the vibrational amplitude applied to the vibrating atom during the Monte Carlo simulation was the sum in quadrature of the amplitude of each of the atoms.

Another consideration in these calculations relates the effect of the orientation of the sample with respect to the detector acceptance angle on the observed intensity. In the present experimental setup, because the angular acceptance of the ESA was only ±0.7°, the ion-beam spot size was much larger than the area on the sample from which scattered ions were detected by the ESA. Therefore, as the angle between the sample and the ESA was rotated, the effective surface area of the sample within the detection region of the ESA was increased by a factor proportional to the cosecant of the angle between the ESA and the plane of the surface. In all the calculations presented here, this correction has been included.

V. DISCUSSION

A. Clean surfaces

1. [1$\bar{1}$2] azimuth

The [1$\bar{1}$2] azimuth yielded the simplest of the ICISS polar scans presented here, since there was only one type of atomic plane involved in the scattering. Thus, these data were used to optimize the parameters in the calculations before modeling the polar scans collected along the other azimuths, which had more complex atomic arrangements. The side view of the [1$\bar{1}$2] azimuth in Fig. 6 shows the three types of atom pairs that contributed most to the observed ICISS polar scan. In Fig. 7, the calculated scattering intensity from each of these alignments is shown. The Firsov screening length in the Molière potential for the one-atom Monte Carlo simulations used in these calculations was reduced by a factor of $C=0.6$. This value for C was found to produce the best agreement between the calculations and experiment. The rms vibrational amplitudes used in these calculations for the second and deeper layers was 0.078 Å, which is the value calculated from a bulk Debye temperature of 343 K.[32] The first-layer vibrational amplitudes were enhanced by a factor of 1.5 over the bulk value, which gave the best agreement between the calculated SFP heights and the experimental data.

Figure 7(a) shows the calculated contribution to the ICISS polar scan for the ions scattered from the first-layer atoms. These scattering events, which produced the SFP for this azimuth, are represented by the trajectory labeled 1s in Fig. 6. Because of the correction that was made for the acceptance area of the ESA, this calculation showed a cosec($\theta_s+14°$) dependence in the region following the SFP. Also, because of the ESA acceptance correction, the height of the SFP was much larger than the height of the flux peaks in the other calculated contributions to the [1$\bar{1}$2] ICISS polar scan.

Figure 7(b) shows the contribution from the second-layer scattering, which displays a flux peak resulting from first- to second-layer shadowing, or trajectory 2 of Fig. 6. This calculation was performed for an inward relaxation of the topmost atomic layer of 10% of an interlayer spacing. Because the atom pair in this atomic alignment was oriented 27.4° from the plane of the surface, the flux peak began at a much higher polar angle than did the flux peak of Fig. 7(a). At incident ion polar angles smaller than 27.4°, there was no scattering from the second layer because it was completely shadowed by the first.

The scattering from the third atomic plane is represented by the trajectories labeled 3s and 3b in Fig. 6, which consists of shadowing of third-layer atoms by second-layer atoms and blocking by first-layer atoms of those ions scattered by the third-layer atoms. In Fig. 7(c) the calculated contributions to the polar scan from each of these events is shown. Despite the differences in the calculation of the shadowing and blocking contributions, the two flux peaks shown in Fig. 7(c) are almost mirror images of each, especially when considering that the analyzer acceptance correction was responsible for the slightly increased intensity of the shadowing flux peak height with respect to the blocking flux peak. The major difference in these contributions to the ICISS polar scan is that they operate in the opposite direction to one another

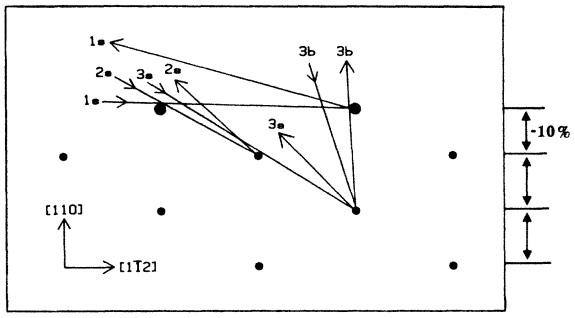

FIG. 6. Side view of the Cu(110) surface region containing the [1$\bar{1}$2] azimuth. Each of the primary trajectories that contributed to the ICISS polar scan taken along this azimuth is shown by a pair of arrows. These arrows are at a 14° angle with respect to each other to indicate the experimental ion-beam-to-detector geometry. The letter s refers to a shadowing atomic alignment and the b to a blocking alignment. The size of the circles represents the mean-square vibrational amplitude of the atoms employed in the calculations. In this model, the first-to-second interplanar spacing has been decreased 10% with respect to the bulk value.

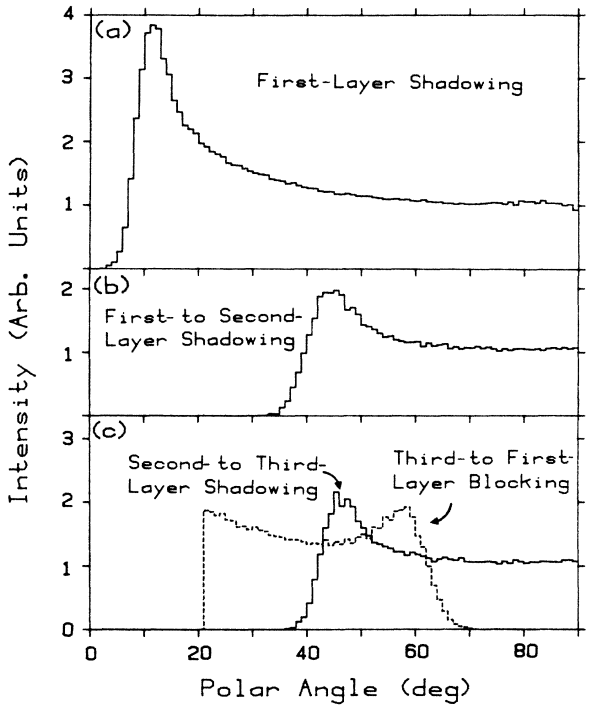

FIG. 7. Calculated contributions to the ICISS polar scan collected along the [1$\bar{1}$2] azimuth. (a) First-layer shadowing (trajectory 1 of Fig. 6), (b) First- to second-layer shadowing (trajectory 2), (c) solid line—second- to third-layer shadowing (trajectory 3s) and dashed line—third- to first-layer blocking (trajectory 3b).

and are offset from each other by an angle that is the difference in angle between the interatomic vectors of the shadowing and blocking atom pairs minus the 14° difference in angle between the ion beam and the analyzer positions. The shape of the largest feature in these ICISS polar scans is thus governed by both shadowing and blocking phenomena, and is very sensitive to the scattering angle employed. If the scattering angle were to be changed, the relative positions of these features would be shifted with respect to one another and the observed ICISS polar scan would be considerably different.

Since these shadowing and blocking effects occur sequentially, the resulting yields should be multiplied by one another to produce the total scattering contribution from the third layer. However, the energy resolution of the ESA restricts the detected part of the scattered-ion yield that results from sequential scattering to ions that scattered at an energy within 15 eV of the true singly scattered ions. Results of various approaches to account for combined shadowing and blocking effects were compared with both string calculations and experimental data. It was found that a reasonable approximation to the ICISS intensity for such situations was to simply use the shadowing intensity from low polar angles up to the polar angle at which the calculated shadowing and blocking fluxes were equal, and then use the blocking intensity for higher polar angles. This procedure produced flux peaks that had the basic overall shape as in the experimental ICISS scans, but the intensities of the flux peaks were not always in agreement. For the purposes of the present analyses, however, it is sufficient to determine the angular position of the flux peaks resulting from subsurface scattering.

The total calculated result is shown as the histogram in Fig. 8, which was produced by summing the results from Figs. 7(a), 7(b), and 7(c), after merging the shadowing and blocking contributions shown in Fig. 7(c) at a polar angle of 52°. The experimental polar scan is shown as a solid line in Fig. 8, as was normalized in intensity with the calculated scan at a polar angle of 90°. This was the most reasonable polar angle for aligning the intensities, since the focusing effects should be minimized at that incident angle. The calculated and experimental ICISS polar scans display the same overall flux peak shapes and agree well on the height and shape of the leading edge of the SFP, but otherwise the experimental polar scan is consistently higher in intensity than the calculated polar scan.

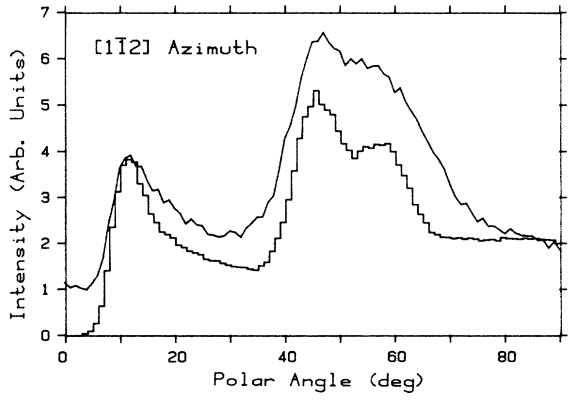

FIG. 8. ICISS polar scan for 5-keV $^6Li^+$ scattering from Cu(110) along the [1$\bar{1}$2] azimuth. The upper solid line is the experimental data and the lower histogram is the result of a calculation. The ordinate refers to the calculated intensity. The experimental intensity was aligned with the calculated intensity at 90°, at which only two atomic planes should contribute to the scattering.

At polar angles below 5°, the excess intensity in the experimental scan was due to scattering from the edge of the sample, as mentioned previously. However, at polar angles greater than 5°, the ion beam was completely on the sample surface, so no scattering from the edge occurred, and the SFP agreed very well with the calculation. The height of the calculated SFP was very sensitive to the vibrational amplitude employed and the agreement with experiment for the height of the SFP was an indication that the value obtained for the enhancement of the surface vibrational amplitude was reasonable.[33]

While the ion beam was at a low polar angle, only the surface atoms contributed to the QS scattering. For this reason, the calculations produced an excellent quantitative agreement with the [1$\bar{1}$2] SFP. As the polar angle increased past the region of the SFP, the experimental intensity was consistently higher than the calculated intensity. Since the intensity normalization of the scans in Fig. 8 was at an angle at which very little flux enhancement should have occurred, the higher intensity of the experimental polar scan indicated that scattering trajectories not included in the calculation contributed to the experimental data. One possibility for such extra scattering trajectories is that scattering could have occurred from atoms other than those in the outermost three layers. Calculations of the shadow and blocking cone sizes, however, showed that there could be no direct scattering from these deeper layers. It was possible, however, for ions to have experienced multiple collisions in order to reach a deeper layer. The possibility also existed for multiple-scattering trajectories that involved interplanar scattering. These multiple-scattering trajectories could still have resulted in an energy close to the QS energy. However, subtracting the calculated from the experimental polar scan yielded a structureless bulge at intermediate ion incidence angles, so the neglected multiple-scattering trajectories did not add any new features to the polar scan, and optimizing structural parameters in the calculation by aligning flux peak positions should yield a valid structure.

A comparison of the energy spectra taken at normal incident [see Fig. 9(a)] and at a polar angle corresponding with a flux peak [see Fig. 9(b)] was consistent with the multiple-scattering explanation of the discrepancy between the calculation and experiment. At normal incidence, the energy spectrum showed a QS peak that was clearly separated from the multiple-scattering background. For incidence at a polar angle that maximized the intensity of a flux peak, however, the QS scattering was indistinguishable from the multiple-scattering background. These energy spectra are qualitatively very similar to energy spectra observed in RBS for channeling and nonchanneling incidence directions.[30] The inability to distinguish a QS peak in the energy spectrum collected at the

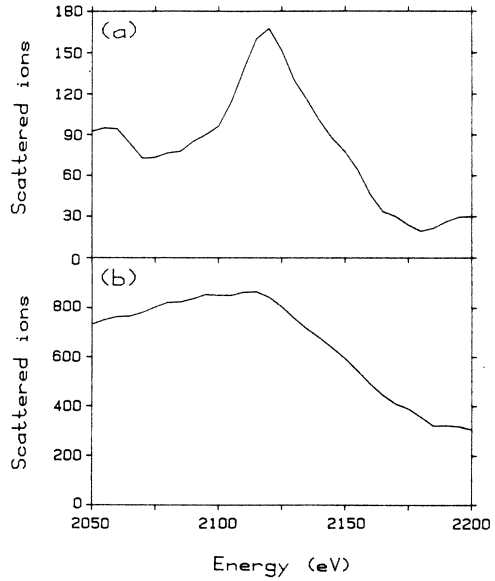

FIG. 9. Energy spectra for 3-keV $^6Li^+$ scattering from Cu(110) at a 162.5° scattering angle. (a) Ion-beam incidence normal to the surface, and (b) ion-beam incidence at a 45.5° polar angle along the [001] azimuth, which represents scattering at a flux peak. Note the difference in the intensity scales for the two spectra.

flux peak orientation showed that there was a significant multiple-scattering signal at the single-scattering energy.

The multiple-scattering contribution to the ICISS scans was small enough that the comparison of the calculations presented here to the experimental data proved valuable in understanding the trajectories primarily responsible for the observed scattering features. Also, since the SFP had essentially no multiple-scattering contribution, a good estimate of the surface vibrational amplitude was obtained. The calculations also showed that the structural model for the Cu(110) surface in which the first layer is relaxed downward is correct. If the outermost layer were bulklike or relaxed outward, then trajectory 3*s* could have not contributed a separate flux peak to the ICISS polar scan and the incident ions could have not been focused by the second layer onto the third, because at the polar angle where this focusing occurs, the second layer would have been shadowed by the first. The same is true for corresponding trajectories observed in the other azimuths. Thus, the appearance of features in the ICISS polar scans corresponding to flux peaks created by these atom pairs is a certain indication that the surface plane is relaxed inwards.

2. [1$\bar{1}$0] azimuth

The calculation for scattering along the [1$\bar{1}$0] azimuth is shown in Fig. 10. This calculation was performed with the same parameters as in the preceding section, but the trajectories included in the calculation were those shown in Fig. 11. For the [1$\bar{1}$0] azimuth, the calculations displayed the same flux peak shapes and locations as did the experimental scan, but the intensity in the experimental scan was higher than the intensity in the calculation at

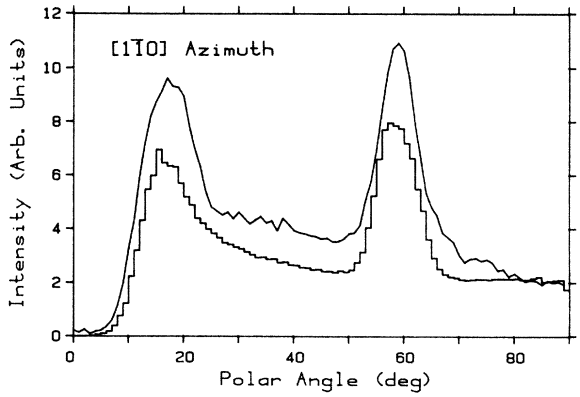

FIG. 10. ICISS polar scan for 5-keV $^6Li^+$ scattering from Cu(110) along the [1$\bar{1}$0] azimuth. Same comments as for Fig. 8.

all polar angles below about 80°.

The calculated and measured SFP's along the [1$\bar{1}$0] azimuth were not in quantitative agreement, although the vibrational amplitude employed for the surface atoms was the same as that used along the [1$\bar{1}$2] azimuth. The reason for the discrepancy in the intensity of the SFP is that the interatomic separation of the atom pairs responsible for the SFP is smaller in this azimuth than in the other azimuths. With a smaller interatomic separation, the possibility for overlapping flux enhancements by shadowing and blocking by the same atom pair exists. This effect occurs when an ion is steered by the first atom onto the second atom, then scattered at a large angle from the second atom, and finally deflected along the exit trajectory by the first atom. Because the first collision is only a small-angle collision, not enough energy is lost by the ion to dislodge the atom from its equilibrium position, so that atom remains to contribute to the blocking flux enhancement during the outward trajectory of the ion.

The simple model used did not account for this combined shadowing and blocking, but separate calculations were used to determine that this effect was indeed occur-

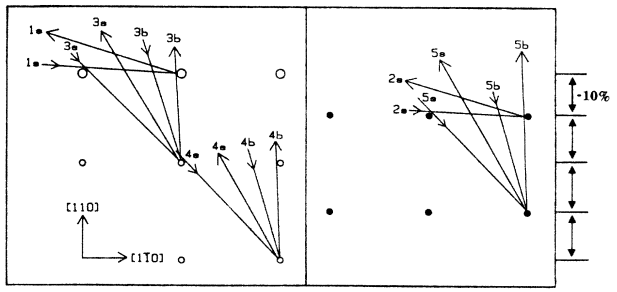

FIG. 11. Side view of the Cu(110) surface region containing the [1$\bar{1}$0] azimuth. The open and closed circles represent atoms in different atomic planes. The plane that is terminated by first-layer atoms is shown in the left panel, while the plane terminated by second-layer atoms is shown in the right. Other comments are as for Fig. 6.

ring. For 5-keV $^6Li^+$ on Cu scattered at 166°, the effect is important when considering an atom pair at a nearest-neighbor separation. The next largest interatomic separation in the Cu crystal structure was determined to be too large for this effect to occur. The combined shadowing and blocking could have been avoided by using a smaller scattering angle, but by reducing the scattering angle other features in the polar scans would have been attenuated. A 166° scattering angle was thus a reasonable compromise for the present ICISS study. The shadowing and blocking effect could also have been responsible for some of the increased intensity of the experimental subsurface flux peaks, collected along this and other azimuths, over the corresponding calculated flux peaks.

The flux peak at ~60° in the ICISS polar scan along the [1$\bar{1}$0] azimuth resulted from different shadowing and blocking flux enhancements that nearly overlapped (trajectories 3*s*, 3*b*, 4*s*, 4*b*, 5*s*, and 5*b* in Fig. 11). Because all these shadowing and blocking flux enhancements appeared at nearly the same polar angle, this flux peak was large and narrow.

3. *[001] azimuth*

The results for scattering along the [001] azimuth are shown in Fig. 12. In this azimuth, there are seven QS trajectories, shown in Fig. 13, that contributed to the observed polar scan. Trajectories 1 through 5 were similar to the five corresponding trajectories in the [1$\bar{1}$0] azimuth. Because of the longer distance between the vertical rows in this azimuth, however, trajectories 6 and 7 were also possible. The interatomic separation of the atom pairs that contributed to the SFP along this azimuth was large enough so that there was no contribution from combined shadowing and blocking in the SFP. Therefore, the calculations produced a quantitative match to the experimental SFP intensity along the [001] azimuth.

As was observed in the other two azimuths, in the region between the SFP and a polar angle of 90°, the intensity in the experiment was consistently higher than the calculated intensity. Unlike the previous two scans, however, the shapes of the remaining flux peaks were not the same

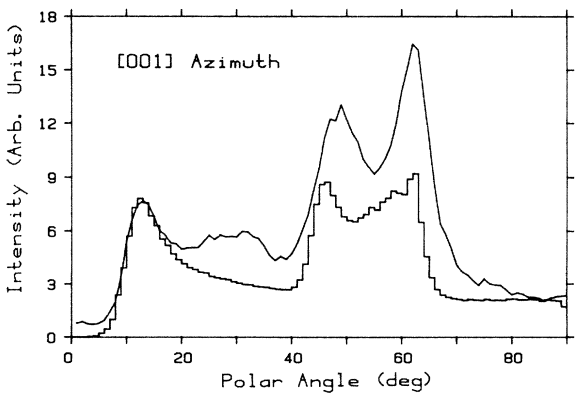

FIG. 12. ICISS polar scan for 5-keV $^6Li^+$ scattering from Cu(110) along the [001] azimuth. Same comments as for Fig. 8.

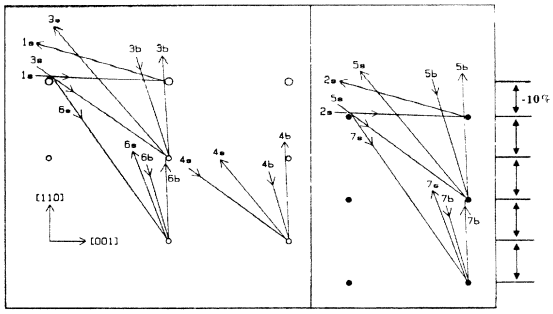

FIG. 13. Side view of the Cu(110) surface region containing the [001] azimuth. Other comments are as for Fig. 11.

in the calculations and experiment. There was a broad feature observed in the experimental scan at about 30° that did not appear in the calculations, and the flux peak at ~47° was shifted in the experimental scan relative to the calculated polar angle. Again, these differences were most likely due to interplanar scattering. Since the crystal is more open in this direction than in the [1$\bar{1}$0] direction, the possibility for out-of-plane multiple scattering is larger.

4. *Wide-area detector*

The polar-angle scans performed with the wide-area detector provide further insight into the multiple-scattering contribution. As seen in Fig. 3, the intensity of the wide-area polar scans., which is dominated by multiply scattered species, displays increased intensity over the ICISS scans in the region for which the experimental ICISS scans were increased in intensity above the calculated ICISS scans. Thus, the broad area of enhanced scattering yield at ~30° polar angle in the experimental ICISS scan of Fig. 12 that does not appear in the calculated yield is probably the result of multiple scattering.

The initial rise in intensity of the wide-area scans occurred at approximately the same polar angle as did the SFP in the corresponding ICISS scans. This is experimental evidence that multiple scattering did not greatly effect the shape of the SFP. At polar angles above the region of the SFP, the wide-area scans show peaks that do not necessarily have a local maximum at the same location as the ICISS flux peaks. Thus, since the ESA is sensitive to a portion of the multiply scattered yield, multiple scattering can influence the shape of the observed flux peaks.

B. Cu(110-(2×1)-O

The ICISS polar scans for 5-keV $^6Li^+$ scattering along the [1$\bar{1}$0] azimuth from the Cu(110) surface exposed to various amounts of oxygen are shown in Fig. 4. After the adsorption of 200 L of O_2, the SFP height decreased with respect to the intensity at 90°, the SFP width broadened, and a new feature appeared in the polar scan at ~38°. As more oxygen was adsorbed onto the surface, the intensity of the SFP decreased further and the feature at 38° was no longer distinguishable.

Calculations were performed for scattering along the

[1$\bar{1}$0] azimuth assuming a missing-row structure. The best agreement between the calculations and the experimental ICISS polar scans, shown in Fig. 14, was obtained for a surface in which the interlayer spacing between the outermost two atomic layers was expanded by (25±10)% and the second- to third-layer spacing was contracted by (10±5)% with respect to the bulk spacings. This is the structure that would result if the top atomic layer were simply added to the relaxed structure that was employed in the clean-surface calculations. For these calculations, only the vibrational amplitudes of the outermost atoms were enhanced over the bulk Cu values by a factor of 1.5, while the remaining layers were modeled using bulk vibrational amplitudes.

A side view of the Cu(110) surface along this azimuth that shows the missing-row model is shown in Fig. 15. There are seven trajectories that contributed to the ICISS polar scan for this structure. The calculational result for the missing-row model is shown as the histogram in Fig. 14, along with experimental data for a 200-L exposure to oxygen. The SFP was composed of trajectories 1 and 2 from Fig. 15. Despite the large differences in the interatomic spacings of the atom pairs involved in these trajectories, the contributing features overlapped so much that a single SFP that was wider than the SFP observed for the clean surface resulted from the calculation. Scattering events similar to that illustrated by trajectory 7*s* of Fig. 15 produced the feature at a polar angle of 38° in Fig. 14. A peak resulting from the same atom pair was observed and explained in terms of a missing-row model by Niehus and Comsa for 2-keV $^{23}Na^+$ on Cu(110)-(2×1)-O.[12] The existence of this peak in the experimental data clearly showed that the missing [001] row model was correct, since the corresponding trajectories could not have been possible if the surface was reconstructed in a buckled-row model.[25,26] The scattered ions would have been blocked from exiting the surface, just as those scattering from the clean surface were (compare Figs. 10 and 11 to 14 and 15, respectively). Thus, the ICISS data display a flux peak that is uniquely related to the existence of missing rows on the Cu surface.

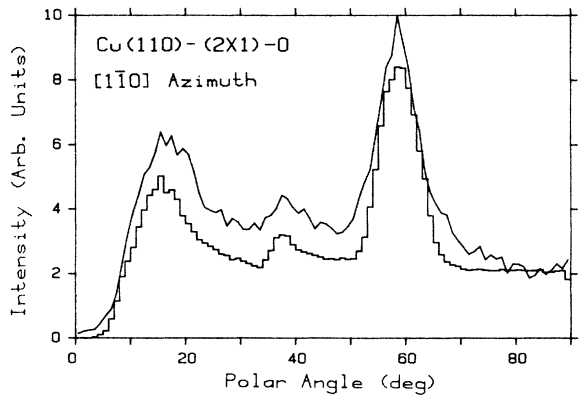

FIG. 14. ICISS polar scan for 5-keV $^6Li^+$ scattering from Cu(110)-(2×1)-O along the [1$\bar{1}$0] azimuth after an exposure to 200 L O_2. Note the existence of the flux peak at a polar angle of 38° and compare with the corresponding scan for the clean surface in Fig. 10. Other comments are the same as Fig. 8.

The calculated angular position of this flux peak was found to be very sensitive to the position of the outermost atomic layer with respect to the third atomic layer, since the feature resulted from first- to third-layer shadowing. Only a relatively large outward relaxation is consistent with the experimentally measured position of this peak. The relative positions of the SFP and the flux peak at 60° were found to be sensitive to the second- to third-layer inward contraction employed in the calculation, and a better agreement was found if this spacing was contracted 10% of a bulk interlayer spacing. The calculated intensity of the 60° flux peak matched the intensity of the experimental flux peak better than in the calculations for the clean surfaces, but this may not be significant considering the complicated nature of this feature.

The most significant point of this analysis is the large expansion of the first interlayer spacing in the missing-row structure. The qualitative assignment of an expansion was dependent only on the location of the experimental feature at 38°. Since the location of this feature resulted from first- to third-layer shadowing, the existence of an outward expansion of the first layer with respect to the third by (15±5)% of a bulk interlayer spacing is fairly certain. Since the uncertainty in determining the second- to third-layer 10% contraction was also on the order of 5%, the uncertainty in determining the first- to second-layer spacing is ±10%. Such a large expansion should not be too surprising, since the adsorbed oxygen atoms have been shown to reside between the first and second layers.[21,23]

It is interesting to note that in the buckled-row model proposed by Feidenhans'l and Stensgaard to explain their RBS results,[25] the best agreement between the experimental data and computer simulations was obtained for a structure in which every other [001] row of Cu surface

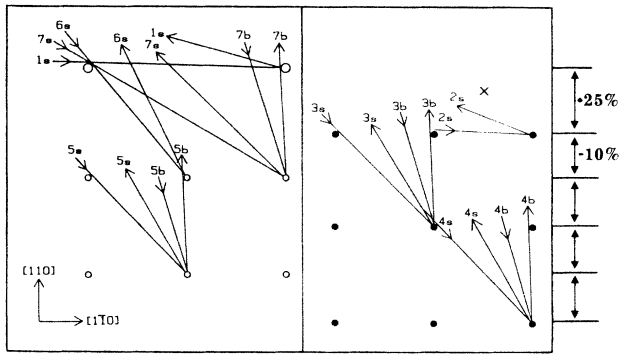

FIG. 15. Side view of the Cu(110) surface region containing the [1$\bar{1}$0] azimuth with the missing-row model. Note especially the trajectory labeled 7*s* in this figure, which gives rise to a flux peak that does not occur for any model other than one in which every other [001] row of atoms is missing. In this model, the first-to-second interplanar spacing is increased 25% with respect to the bulk, and the second-to-third is contracted 10%. The *x* marks the location proposed in Refs. 21–23 for the adsorbed oxygen atoms. Other comments are as for Fig. 11, to which this figure should be compared.

atoms was displaced outwards by 21% of a bulk interplanar spacing, while the remaining [001] rows were within a few percent of the bulk positions. The agreement between the positions of the outward displaced [001] rows of Ref. 25 and the present study is reasonable because RBS is very sensitive to the positions of atoms that are not located at bulk lattice sites, such as the topmost atoms of the Cu(110)-(2×1)-O surface. However, the results of Ref. 25 also indicated a small expansion of the second to third atomic layer, which is in contradiction with the present results.

A related surface, Ni(110)-(2×1)-O, has also been explained in terms of a missing-row model in which every other [001] Ni row is vacant.[34,35] Smeenk *et al.* examined the Ni(110) and Ni(110)-(2×1)-O surfaces using RBS[34] and discussed the history behind the study of these surfaces. For the clean Ni(110) surface, the results of Ref. 34 indicated an inward relaxation. Upon oxygen adsorption, however, the first- to second- and second- to third-layer spacings in the missing-row structure were interpreted as being within 0.1 Å of the bulk lattice positions.

In the analysis of the data presented in this paper, the effect of the oxygen atoms on the observed ICISS polar scans has been ignored up to this point. Although scattering directly from the oxygen atoms would not be observed because the ESA was set to the energy corresponding with QS scattering from Cu, the oxygen atoms can act to block ions scattered from Cu atoms from reaching the detector, or can create additional flux peaks by forming a shadow cone that can interact with a Cu atom. LEIS studies[21–23] have suggested that the oxygen atoms reside at the point marked with an *x* in Fig. 15, which is along the plane of Cu atoms that is terminated by the second layer. Thus, the oxygen atoms could interfere only with trajectories 2, 3, and 4 of Fig. 15. Calculations of the same type used for the Cu shadow-cone flux enhancements were employed to determine the effect that oxygen atoms located at the positions equivalent to those in Fig. 15 would have on the ICISS scans. These calculations indicated that the shadowing flux enhancement due to the oxygen atoms was minimal, because of the small scattering cross section and large vibrational amplitude that an oxygen atom would have with respect to Cu.

In the polar scans collected after the sample was exposed to 600 and 1200 L of oxygen, the SFP and the 38° feature disappeared. The ICISS scan collected after a 1200-L exposure was very similar to that observed from a disordered Cu(110) sample,[27] which indicates that the presence of additional oxygen above the amount required to produce a missing-row structure creates disorder of some unknown kind in the surface-layer Cu. In Ref. 21, a secondary oxygen adsorption site was proposed that is in the same plane as the oxygen marked with an *x* in Fig. 15. If both of these adsorption sites were saturated, then the scattering from the second atomic layer, trajectory 2*s* in Fig. 15, would be greatly attenuated. Because the largest contribution to the SFP in the missing-row structure is trajectory 2*s*, this saturated oxygen coverage could be responsible for the observed attenuation of the SFP. However, if only the second atomic layer were affected, the flux enhancement from the missing-row trajectories 1*s* and 7*s* would still have contributed to the observed polar scan. Because of the larger interatomic spacing of the atom pair, the flux enhancement from trajectory 1*s* occurs at a lower polar angle than does the enhancement from trajectory 2*s*. In the experimental scans of Fig. 4, as the oxygen exposure was increased, the onset of the scattering shifted towards higher polar angles, indicating that in addition to the attenuation of trajectory 2*s*, the contribution from trajectory 1*s* was also decreased. This observation, in conjunction with the observation that the feature at 38° that resulted from trajectory 7*s* was also attenuated, is evidence that the Cu(110) surface layer was disordered by the presence of the additional oxygen above the required to produce an ordered missing-row structure.

VI. CONCLUSIONS

ICISS polar scans were recorded for the scattering of 5-keV $^6Li^+$ from Cu(110) and Cu(110)-(2×1)-O. These scans all displayed flux peaks that corresponded to the enhanced flux at the edge of shadow or blocking cones. One-atom Monte Carlo calculations, in which only shadowing and blocking within one atomic plane were considered, were performed to model the expected shape of an ICISS polar scan. By adjusting the structural parameters in a calculation of an ICISS scan for a particular model of a surface, a quantitative determination of these parameters was obtained.

The calculations reproduced the experimental peak shapes and locations, but the experimental data were always either equal to or higher in intensity than the calculations. This implied that the calculations were correct in attributing intensity to certain ion trajectories, but were not able to account for all of the possible multiple-scattering trajectories that could lead to scattering at the QS energy. However, the multiple scattering did not contribute any new peaks that interfered with a structural determination, and the most important part of the data analysis was to match the peak locations of the calculated to the experimental scans.

The vibrational amplitudes of the atoms in the outermost layer of the Cu surfaces were found to be enhanced by a factor of 1.5 over the bulk vibrational amplitude. Additionally, structural information was obtained to within 0.1 Å. For the outermost atomic layer of Cu(110), an inward relaxation of (10±5)% of a bulk interlayer spacing was determined, in agreement with previous studies. When oxygen was adsorbed onto the sample, a sharp 2×1 LEED pattern was observed for exposures from 200 to 1200 L. For a 200-L exposure, the oxygen induced a reconstruction of the Cu surface that was interpreted as a missing-row structure in which every other [001] row of Cu atoms was vacant; the results were not consistent with a buckled-row model. The first- to second-layer spacing of this surface was shown to be expanded with respect to the bulk lattice spacing by (25±10)%, while the second to third layer was contracted by (10±5)%. The positions of these atomic planes are the new structural results determined by this study. Since the angular location of the ICISS features was consistent with the accepted model for

the clean Cu(110) surface, the evidence for the outward relaxation of the Cu(110)-(2×1)-O surface after a 200-L oxygen exposure is very strong.

For larger oxygen exposures, ICISS showed that most of the surface was disordered, even though the LEED pattern was still sharp and clear. Thus, one must be very careful in comparing structural studies of this surface to know the O_2 exposure. ICISS is seen to be an extremely powerful technique, not only for determining structural parameters, but also for sensing surface disorder.

ACKNOWLEDGEMENTS

This project was supported by the National Science Foundation (NSF) under Grant No. DMR-82-04858. In addition, the computations were performed on a computer purchased in part with funds supplied by NSF Grant No. CHE-79-10965. R.S.W. acknowledges the Camille and Henry Dreyfus Foundation and the Alfred P. Sloan Foundation for partial support. J.A.Y. acknowledges the IBM Corp. for partial support.

---

*Present address: IBM Thomas J. Watson Research Center, Yorktown Heights, NY 10598.

†Present address: Department of Chemistry, University of Hawaii, Honolulu, HI 96822.

[1]D. P. Smith, Surf. Sci. **25**, 171 (1971).

[2]T. M. Buck, in *Methods of Surface Analysis,* edited by A. W. Czanderna (Elsevier, Amsterdam, 1975), p. 75.

[3]Taglauer and W. Heiland, Surf. Sci. **33**, 27 (1972).

[4]H. H. Brongersma and P. M. Mul, Surf. Sci. **35**, 393 (1973).

[5]A. L. Boers, Surf. Sci. **63**, 475 (1977).

[6]R. P. N. Bronkers and A. G. J. DeWit, Surf. Sci. **104**, 384 (1981).

[7]H. Niehus and E. Bauer, Surf. Sci. **47**, 222 (1975).

[8]M. Aono, C. Oshima, S. Zaima, S. Otani, and Y. Ishizawa, Jpn. J. Appl. Phys. **20**, L829 (1981).

[9]M. Aono, Y. Hou, C. Oshima, and Y. Ishizawa, Phys. Rev. Lett. **49**, 567 (1982).

[10]M. Aono, Y. Hou, R. Souda, C. Oshima, S. Otani, Y. Ishizawa, K. Matsuda, and R. Shimizu, Jpn. J. Appl. Phys. **21**, L670 (1982).

[11]R. Souda, M. Aono, C. Oshima, S. Otani, and Y. Ishizawa, Surf. Sci. **128**, L236 (1983).

[12]H. Niehus and G. Comsa, Surf. Sci. **140**, 18 (1984).

[13]E. Bøgh, in *Channeling,* edited by D. V. Morgan (Wiley, New York, 1973), p. 435.

[14]E. Taglauer, W. Englert, W. Heiland, and D. P. Jackson, Phys. Rev. Lett. **45**, 740 (1980).

[15]J. A. Yarmoff and R. S. Williams, Surf. Sci. (to be published).

[16]L. K. Verhey, B. Poelsma, and A. L. Boers, Nucl. Instrum. Methods **132**, 565 (1976).

[17]I. Stensgaard, R. Feidenhans'l, and J. E. Sørensen, Surf. Sci. **128**, 281 (1983).

[18]D. L. Adams, H. B. Nielsen, and J. N. Andersen, Surf. Sci. **128**, 294 (1983).

[19]H. L. Davis, J. R. Noonan, and L. H. Jenkins, Surf. Sci. **83**, 559 (1979).

[20]J. R. Noonan and H. L. Davis, Surf. Sci. **99**, L424 (1980).

[21]R. P. N. Bronckers and A. G. J. DeWit, Surf. Sci. **112**, 133 (1981).

[22]Th.M. Hupkens and J. M. Fluit, Surf. Sci. **143**, 267 (1984).

[23]A. G. J. DeWit, R. P. N. Bronckers, and J. M. Fluit, Surf. Sci. **82**, 177 (1979).

[24]J. Lapujoulade, Y. Le Cruër, M. Lefort, Y. Lejay, and E. Maurel, Surf. Sci. **118**, 103 (1982).

[25]R. Feidenhans'l and I. Stensgaard, Surf. Sci. **133**, 453 (1983).

[26]R. A. DiDio, D. M. Zehner, and E. W. Plummer, J. Vac. Sci. Technol. A **2**, 852 (1984).

[27]J. A. Yarmoff and R. S. Williams, Surf. Sci. (to be published).

[28]J. S. Ahearn, Jr., J. P. Monaghan, Jr., and J. W. Mitchell, Rev. Sci. Instrum. **41**, 1853 (1970).

[29]J. A. Yarmoff and R. S. Williams, Rev. Sci. Instrum. (to be published).

[30]W. K. Chu, J. M. Mayer, and M. A. Nicolet, *Backscattering Spectrometry* (Academic, New York, 1978).

[31]J. A. Yarmoff and R. S. Williams, Surf. Sci. **127**, 461 (1983).

[32]C. Kittel, *Introduction to Solid State Physics,* 5th ed. (Wiley, New York, 1976).

[33]J. A. Yarmoff and R. S. Williams, J. Vac. Sci. Technol. **A** (to be published).

[34]R. G. Smeenk, R. M. Tromp, and F. W. Saris, Surf. Sci. **107**, 429 (1981).

[35]H. Niehus and G. Comsa, Surf. Sci. **151**, L171 (1985).